

PAPER

CrossMark
click for updatesCite this: *RSC Adv.*, 2016, 6, 24976

Isotype heterostructure of bulk and nanosheets of graphitic carbon nitride for efficient visible light photodegradation of methylene blue

Biswajit Choudhury^a and P. K. Giri^{*ab}

Nanosheets of g-C₃N₄ were prepared by the ultrasonic treatment of aqueous dispersed bulk C₃N₄ for 10 h. The nanosheets have a comparatively larger surface area (121 m² g⁻¹) than that of bulk C₃N₄ (18 m² g⁻¹). Bulk C₃N₄ prepared by direct heating of urea has a band gap of 2.74 eV, whereas the nanosheets of g-C₃N₄ exhibited an enlarged band gap of 2.97 eV. The isotype heterostructure is fabricated by the solid-state mixing of bulk and nanosheets of C₃N₄ followed by ultrasonic treatment for dispersion. The heterostructure shows an effective band gap of 2.62 eV with an average charge carrier lifetime of 21 ns, which is longer than that of the bulk (13.2 ns) or nanosheets (17.4 ns) of g-C₃N₄. The heterostructure exhibits significantly higher visible light photocatalytic activity in the degradation of methylene blue (MB) over bulk or nanosheets of g-C₃N₄. The superior photocatalytic performance of the heterostructure is ascribed to band-bending at the interface that promotes molecular exciton dissociation and facilitates facile separation of charge carriers at the interface. From the results of photocatalysis, it is speculated that the photogenerated [•]OH radicals in conjunction with [•]H atoms take part in photocatalysis by *N*-deethylation followed by aromatic ring cleavage of the MB molecule.

Received 12th January 2016
Accepted 28th February 2016

DOI: 10.1039/c6ra00933f

www.rsc.org/advances

1. Introduction

Heterogeneous photocatalysis based on TiO₂ has been researched for a few decades, owing to its stable photochemical reactions in the detoxification of air/water pollutants and H₂ generation by water splitting by utilizing the UV part of solar spectrum.^{1,2} Practical applications of TiO₂ are substantially compromised by its wide band gap with limited or no visible absorption. Recently, a metal free polymeric semiconductor, graphitic carbon nitride (g-C₃N₄), has drawn immense interest because of its promising applications in H₂ generation, photodegradation of organic pollutants, and possible optoelectronic applications.^{3–5} The basic unit of g-C₃N₄ is the tri-*s*-triazine unit (or *s*-heptazine) with a strong C–N covalent bond, and the layers in g-C₃N₄ are connected *via* van der Waals interactions.^{6,7} The electronegativity difference between C and N in the *s*-heptazine ring could possibly results in the opening up of a band gap in g-C₃N₄, and as reports predict the measured bulk band gap of g-C₃N₄ is ~2.7 eV with valence and conduction band edge comprising of N 2p lone pair orbital and C 2p orbital, respectively.^{8,9} The preparation method of g-C₃N₄ is simple and involves pyrolysis of nitrogen rich precursors, *viz.*, cyanamide, thiourea, urea at different processing temperatures.¹⁰ Although

the thermally processed g-C₃N₄ shows visible light photocatalytic activity, it exhibits less surface area, only marginal absorption in visible region and suffer from high probability of bulk recombination of photoexcited charge carriers.¹¹ Ultrathin nanosheets of g-C₃N₄ are fabricated by liquid phase exfoliation in solvents *n*-methyl pyrrolidone, 2-propanol, water, *etc.*¹² The nanosheets have tunable absorption and prolonged carrier lifetime, but shows an enlargement in band gap with respect to bulk C₃N₄.^{13,14} As such, for practical applications, the optical absorption in g-C₃N₄ should be improved with narrowed band gap and prolonged lifetime of charge carrier separation. This is indeed achieved by introducing heteroatoms (B, S, O) and constructing heterostructures with other semiconductors (*e.g.* ZnO) with interface mediated charge carrier separation.^{4,15,16} In case of doping, control of doping is a necessary step; otherwise dopants itself may act as carrier recombination center. In contrast, in case of hybridization with inorganic semiconductors proper band alignment and interface formation is essential for efficient charge separation.

Zhang *et al.*¹⁷ developed a metal free isotype heterostructure by the pyrolysis of mixtures of thiourea (S, N, C source) and urea (C, N source). The as-formed heterostructure exhibited very high photocatalytic activity because of different band alignment at the interface promoting charge separation. Dong *et al.*¹⁸ constructed type I and type II isotype heterostructure with different band alignment at the interface, and studied the influence of band bending and charge carrier separation on the effective photocatalytic removal of NO pollutant from air. The benefit of

^aDepartment of Physics, Indian Institute of Technology Guwahati, Guwahati 781039, India. E-mail: giri@iitg.ernet.in

^bCenter for Nanotechnology, Indian Institute of Technology Guwahati, Guwahati 781039, India

constructing heterostructure of $g\text{-C}_3\text{N}_4$ with graphene or other metal oxides has also been considered useful for several energy and environmental applications.¹⁹ In the present study, we have developed an isotype heterostructure starting with the same urea precursors. Initially, bulk $g\text{-C}_3\text{N}_4$ is prepared by thermal condensation of urea. The product is subjected to aqueous phase ultrasonication treatment to yield nanosheets of $g\text{-C}_3\text{N}_4$. Bulk and nanosheets of $g\text{-C}_3\text{N}_4$ are mixed by solid-state mixing and ultrasonically treated to obtain isotype-heterostructure of $g\text{-C}_3\text{N}_4$. Bulk, nanosheet and heterostructure samples are characterized with XRD, FTIR, UV-vis, photoluminescence (PL) spectroscopic techniques. Aqueous exfoliated C_3N_4 nanosheets exhibit very good photodegradation of MB, because of its high surface area and largely separated charge carriers than that of bulk C_3N_4 . Interestingly, heterostructure shows impressively higher absorption in visible region due to effectively lower band gap, and prolonged separation of charge carriers with excellent photocatalytic activity as compared to bulk or nanosheets of $g\text{-C}_3\text{N}_4$.

2. Experimental details

2.1 Preparation of bulk, nanosheets and isotype heterostructure of $g\text{-C}_3\text{N}_4$

(a) **Preparation of bulk $g\text{-C}_3\text{N}_4$.** For the preparation of C_3N_4 , 10 g of urea was taken in a beaker and heated until it was completely dry. The dried white powder was grounded in an agate mortar and taken in a silica crucible covered with a lid. The crucible with powder was calcined at 570 °C for 3 h. The heating rate was 5 °C min^{-1} and the cooling rate was 10 °C min^{-1} . The resultant powder is yellowish in color and is labeled as BCN (bulk carbon nitride).

(b) **Preparation of graphitic carbon nitride nanosheet.** We have adopted aqueous phase exfoliation method for the preparation of carbon nitride nanosheet.²⁰ 500 mg of bulk graphitic carbon nitride was taken in a beaker with 100 mL water. The solution was stirred for 1 h and then transferred to a simple bath ultrasonicator. The solution was ultrasonicated for 10 h. During ultrasonication the surrounding water is warmed up. To maintain the temperature near room temperature, ice cubes were added to water at regular intervals of time. Aqueous dispersed carbon nitride nanosheet was centrifuged at 5000 rpm. The supernatant was again centrifuged at 18 000 rpm to obtain graphitic carbon nitride nanosheet. The sample was labeled as NCN (nanosheets of $g\text{-C}_3\text{N}_4$).

(c) **Preparation of homo-composite (isotype heterostructure) of $g\text{-C}_3\text{N}_4$.** Isotype heterostructure was formed by the combination of BCN and NCN. For the preparation, equal weight ratio (1 : 1) of BCN and NCN was grounded in an agate mortar. Solid state mixing in agate mortar was continued for 1 h. The mixture of BCN and NCN was transferred to a beaker. Then 100 mL H_2O was added to the beaker and stirred for 1 h. The stirred mixture was then transferred to an ultrasonicator and ultrasonicated for 1 h. After ultrasonication the mixture was naturally dried at 70 °C. This as-prepared sample was labeled as BCN-NCN.

2.2 Characterization details

High resolution X-ray diffraction (XRD) pattern was obtained in a Bruker D8 focus AXS X-ray diffractometer equipped with a Cu $K\alpha$ source of $\lambda = 1.54 \text{ \AA}$. Morphology of prepared nanosheet was monitored in ZEOL JEM 200 kV transmission electron microscope. Fourier transform infrared spectroscopy (FTIR) was performed in a Nicolet I-410 FTIR spectrophotometer using KBr pellet. N_2 adsorption-desorption isotherm was obtained at 77 K in a Quantachrome iQ autosorb analyzer. For the determination of surface area and pore size distribution from the isotherm, we followed multipoint Brunauer-Emmett-Teller (BET) method and Barrett-Joyner-Halenda (BJH) model, respectively. UV-vis diffuse reflectance (DRS) spectra were recorded in Shimadzu 2450 UV-vis spectrophotometer. Steady state photoluminescence (PL) spectra were recorded in Fluoromax-4 (Horiba Scientific) spectrophotometer. Time resolved photoluminescence (TRPL) analysis was carried out in picosecond time resolved luminescence spectrometer (Edinburg Instruments, Model: FSP920). TRPL data was obtained by exciting the sample at 375 nm.

2.3 Photocatalytic activity study

Photodegradation of methylene blue (MB) by $g\text{-C}_3\text{N}_4$ was studied by monitoring the decrease in the initial concentration of MB solution on exposure to visible light (250 W) for different time intervals. Photocatalytic reaction was performed by dispersing 30 mg of $g\text{-C}_3\text{N}_4$ catalyst in 100 mL MB solution with an initial MB concentration of 8 mg L^{-1} . Before visible light exposure, MB solution with catalyst was stirred in dark for 45 min. This allowed complete adsorption of dye molecule on the $g\text{-C}_3\text{N}_4$ surface and equilibrated the adsorption-desorption process on the catalyst surface. Absorption measurement of blank and catalyst loaded MB solution was measured in absence of light. The reactant solution was then placed at a distance of 5 cm from the visible light source (390–730 nm). Light exposure on the MB solution was continued for 90 min. After each 15 min interval, 10 mL of the MB solution was taken out and centrifuged. The suspension was kept for absorption measurement in a UV-vis spectrophotometer. Decrease in the maximum absorption of MB at 664 nm with irradiation time indicates decomposition of MB. We also performed photocatalytic test for blank MB solution without any catalyst for same irradiation time of 90 min. The degradation (D) of MB can be calculated by using following the equation:

$$\% D = \frac{C_0 - C_t}{C_0} \times 100, \quad (1)$$

where C_0 is initial concentration of dye solution and C_t is concentration of MB after irradiation of time t .

2.4 Photocatalyst reusability test

The stability of $g\text{-C}_3\text{N}_4$ as a photocatalyst was tested by repeating the photocatalytic process of recovered photocatalyst. After the initial photocatalytic reaction, the centrifuged product of the catalyst (as mentioned in photocatalytic activity study above) was recovered and dried at 50 °C, and then re-dispersed in fresh

MB solution. The photocatalytic reaction was started and after each cyclic run the catalyst was recovered, dipped in fresh MB solution and irradiated for 90 min. The concentration change of MB was measured with UV-vis spectroscopy at its ~ 664 nm absorption peak. The process was repeated for 3 times. We tested XRD pattern of the catalyst after the 3rd photocatalytic run and compared it with that of the pure catalyst to observe any degradation in the catalyst quality after catalytic reaction.

2.5 Radical trapping experiment

Presence of active radical species and their role on photocatalysis was tested by trapping the active radicals by using some sacrificial agents. Ammonium oxalate (AO), *tert*-butanol (*t*-BA) and *p*-benzoquinone (BQ) were used as hole (h^+), hydroxyl radical scavenger ($\cdot OH$) and superoxide radical ($O_2^{\cdot -}$) scavenger, respectively. The experimental procedure involves addition of 1 mM of scavengers to catalyst–dye solution (30 mg, 8 mg L^{-1}) in 100 mL beaker. For each of the quenchers (*tert*-BA, AO and BQ) three experiments were conducted. The MB-catalyst-quencher was then exposed to visible light for different irradiation time, and the changes in the concentration of MB were monitored at 664 nm in a UV-vis spectrophotometer.

3. Results and discussion

3.1 Structural studies

XRD pattern of BCN, NCN and BCN–NCN are shown in Fig. 1. The samples display an intense (002) diffraction peak at $2\theta = 27.25^\circ$. This peak corresponds to interlayer stacking of aromatic CN unit with $d = 3.27$ Å.^{4,8} Interestingly, the enhancement of (002) peak intensity in NCN demonstrates an improvement in crystallinity after liquid exfoliation of BCN. There is a slight shift in (002) peak position from 27.25° in BCN to 27.74° in NCN, with a corresponding lowering of stacking distance from $d = 3.27$ Å to $d = 3.21$ Å. There is, however, a lowering in (002) peak intensity in BCN–NCN with a corresponding d -spacing of 3.23 Å. The lowering of peak intensity is possibly due to the conjugation of two systems (BCN and NCN) with different degree of crystallinity. All the samples display another low intensity diffraction peak at $2\theta = 13.5^\circ$, corresponding to in-plane ordered tri-*s*-triazine (*s*-heptazine) units having crystal-line plane (100).^{3,4,8} As observed from Fig. 1, there is no obvious

change in the intensity or position of this peak in NCN and in BCN–NCN. For the (100) peak, the interlayer spacing of $d = 6.75$ Å specifies hole-to-hole distance of the nitride pores in $g-C_3N_4$ or intraplanar size of tri-*s*-triazine unit.³ The basic unit structure of graphitic $g-C_3N_4$ is shown in inset of Fig. 1.

Morphological features of BCN, NCN and BCN–NCN are shown in Fig. 2. TEM images of BCN (Fig. 2a) show thick layered structures, which seems to get thinner in NCN with porous structures (Fig. 2b). The honeycomb like porous structures are formed by the release of NH_3 and CO_2 gases during condensation of urea. Initially soft bubbles are formed on calcination, indicating the starting of the release of these gases from urea. These bubbles finally burst out and forms porous structures of C_3N_4 on condensation of urea.²¹ TEM images of NCN obtained at different locations show thick and thin region of the layers (Fig. 2c). As evident from Fig. 2d, there are overlapping layers of BCN and NCN in the heterostructure constituting of bulk (BCN) and nanosheets (NCN) of $g-C_3N_4$. Fig. 2e shows another TEM image taken at a different location of the BCN–NCN sample. The image contains two regions, and we suppose that the thick BCN layers covers up few portion of thin NCN layers. The high resolution image taken on another location shows some folded structure and porous sheet (see Fig. 2f). Formation of paper-fold structure in the nanosheets of $g-C_3N_4$ has been reported by Dong *et al.*²² Chemical structures of BCN, NCN and BCN–NCN are further investigated with FTIR (see Fig. 3a). The samples show an intense absorption band at 808 cm^{-1} corresponding to breathing mode of aromatic ring of carbon nitride.²³ Absorption bands at $1200\text{--}1600\text{ cm}^{-1}$ are assigned to typical symmetric stretching, asymmetric vibrations of C–N–C and C–NH–C units in aromatic ring.^{12,13,22} The broad absorption bands at $3000\text{--}3400\text{ cm}^{-1}$ are attributed to uncondensed primary amine ($-NH_2$) or an imine ($-CH=NH$) and absorbed hydroxyl groups.²³ Fig. 3b shows the N_2 adsorption–desorption isotherm of the samples. The surface area of BCN, NCN and BCN–NCN determined from the isotherm by multipoint BET method are $18\text{ m}^2\text{ g}^{-1}$, $121\text{ m}^2\text{ g}^{-1}$ and $62\text{ m}^2\text{ g}^{-1}$, respectively.

3.2 Optical studies

Changes in optical properties of bulk, nanosheets and heterostructure of $g-C_3N_4$ are investigated with UV-vis absorption spectroscopy. As depicted in Fig. 4, in comparison to BCN the absorption edge is blue shifted in NCN. The UV absorption edge of BCN–NCN is slightly extended to the visible region. Interestingly, NCN and BCN–NCN contain additional absorption in visible region (between 450–700 nm) which is otherwise absent in BCN. The maximum absorption in the ultraviolet (UV) region involves $\pi \rightarrow \pi^*$ electronic transition, and the second narrow absorption in UV is due to $n \rightarrow \pi^*$ transition.^{24,25} This $n \rightarrow \pi^*$ transition is found to be responsible for the visible absorption at 450–700 nm. Several such $n \rightarrow \pi^*$ transitions are possible in $g-C_3N_4$ involving N 2p lone pair orbital (n), and these transitions favor distortion of planarity of *s*-heptazine ring of $g-C_3N_4$.^{14,26} Chen *et al.* have discussed the redistribution of electron density resulting from the distortion of heptazine ring, and the distortion of the ring favor several $n\text{--}\pi^*$ optical transitions (shown inside in

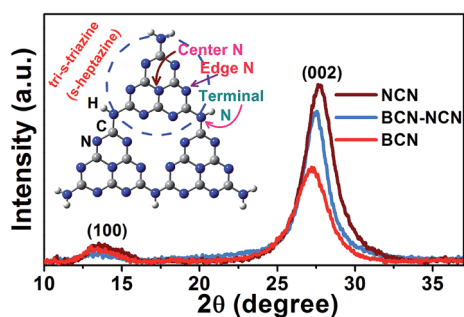


Fig. 1 XRD pattern of BCN, NCN and BCN–NCN. Inset shows the *s*-heptazine unit of $g-C_3N_4$.

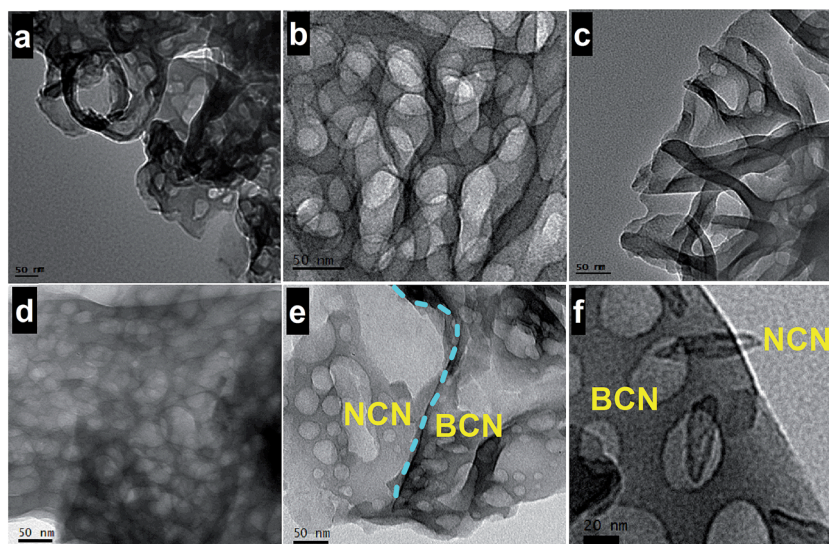


Fig. 2 TEM images of (a) BCN (b and c) NCN and (d–f) BCN–NCN heterostructure.

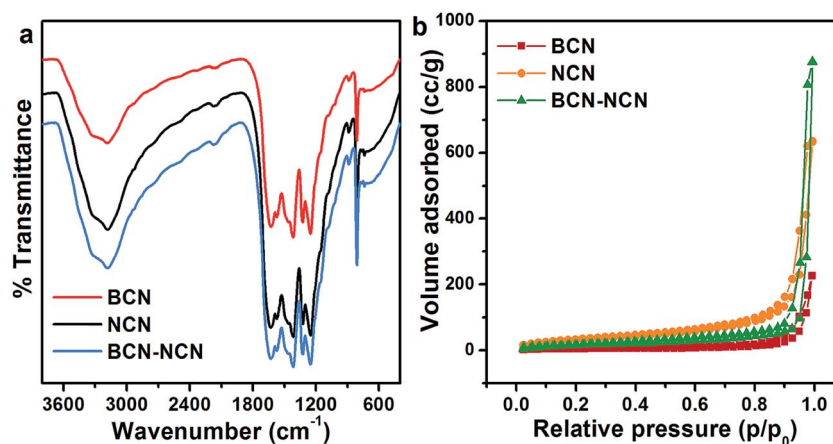


Fig. 3 (a) FTIR spectra and (b) N_2 adsorption–desorption isotherm of BCN, NCN and BCN–NCN.

Fig. 4a).¹⁴ The band gap of each sample is determined by plotting $(Ah\nu)^{1/2}$ vs. $h\nu$, where A is the absorbance. The plotted graph is shown in Fig. 4b and the resulting band gap values are presented in Table 1. The indirect band gap of BCN (2.74 eV) is enlarged to 2.97 eV in NCN. In NCN the stacking distance of the layers decreases and the layers are densely packed. Considering this, the enlargement in band gap in NCN can be attributed to quantum confinement of electrons.¹³ The heterostructure BCN–NCN has an effective band gap of 2.62 eV, and the observed effective band gap could be due to the band edge shift caused by the electronic coupling of BCN and NCN. We speculate that different extent of electronic coupling between BCN and NCN at the interface in the heterostructure and possible band bending at the heterostructure interface could have resulted in the observed reduction in the effective band gap of BCN–NCN. PL spectra of BCN, NCN and BNC-NCN are displayed in Fig. 4c. BCN displays a single broad emission peak at 490 nm. This peak is blue shifted to 465 nm in NCN. BCN–NCN has an emission peak at 483 nm,

which is near the emission peak of BCN. These emissions could be assigned to $\pi^* \rightarrow n$ transition.^{24,25,27} The shift in the peak position results from the change in the packing of the layered structures in the samples that allows electron–hole recombination of π^* electrons with holes in the n orbitals (*e.g.* n_1, n_2, n_3 etc.), which is in conformity with the results of UV-vis spectroscopy. Merschjann *et al.* attributed the $\pi^* \rightarrow n$ emission to molecular exciton generated in the *s*-heptazine ring.²⁸ The efficiency of charge carrier recombination giving rise to the excitonic emission would possibly be different in BCN, NCN and BCN–NCN. To understand the carrier recombination dynamics, we performed time resolved photoluminescence (TRPL) measurements of the samples. Fig. 4d shows the TRPL curves for different samples. It is found that the tri-exponential fitting can best fit the experimental decay curves and the decay components (τ_1, τ_2, τ_3) and relative amplitudes of the decay species (A_1, A_2, A_3) are shown in Table 1. As it is seen in Table 1, first decay component (τ_1) is prolonged in NCN and BCN–NCN as compared to that in BCN,

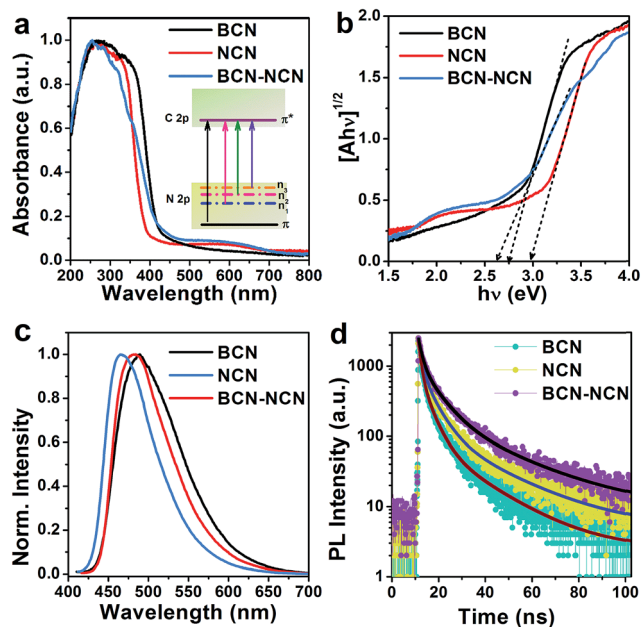


Fig. 4 (a) UV-vis absorption spectra of different samples with inset showing electronic transitions involving N 2p and C 2p orbital. (b) Band gap determination of samples BCN, NCN and BCN-NCN using Tauc plot. (c) Steady state photoluminescence spectra of the samples at an excitation of 375 nm. (d) Time resolved photoluminescence spectra of the samples excited at 375 nm and monitored at emission wavelength 490 nm (BCN), 465 nm (NCN) and 483 nm (BCN-NCN), respectively.

but the relative percentage of these species are lower than BCN. Consideration of second decay component (τ_2) of carrier lifetime with their relative abundance reveal that the corresponding value increases in NCN and BCN-NCN as compared to BCN. Impressively, the third component of lifetime (τ_3) and percentage amplitude of this component (A_3) increases from 18.8 ns (19%) in BCN to 23.3 ns (25%) and 26.8 ns (32%) in NCN and BCN-NCN, respectively. The average lifetime (t_{av}), determined using the

$$\text{formula } t_{av} = \frac{\sum_{i=1}^3 A_i \tau_i^2}{\sum_{i=1}^3 A_i \tau_i}, \text{ increases from 13.2 ns in BCN to 17.4 ns}$$

in NCN and raises to 21 ns in BCN-NCN. The different decay components of carrier lifetime and their relative abundance in the three samples could be linked with bulk or thin layered structures as well as presence of buckling sites, presence of

Table 1 Summary of the band gap calculated from Tauc plot and lifetime of charge carriers in BCN, NCN and BCN-NCN

Sample	Band gap (eV)	Lifetime of carriers			t_{av} (ns)
		τ_1 (ns) ($A_1\%$)	τ_2 (ns) ($A_2\%$)	τ_3 (ns) ($A_3\%$)	
BCN	2.74	1.03 (43)	4.3 (38)	18.8 (19)	13.2
NCN	2.97	1.34 (33)	5.5 (42)	23.3 (25)	17.4
BCN-NCN	2.62	1.60 (27)	7.1 (41)	26.8 (32)	21.0

terminal groups and localized states linked with nitrogen or carbon related defects.^{13,25,27,29} The longest decay components, its high abundance and the longest average lifetime in BCN-NCN could be associated with the interface mediated carrier separation process in the heterostructure formed between BCN-NCN. Possibly the band bending at the interface of the heterostructure formed between BCN and NCN provides the driving force for the efficient carrier separation and long carrier lifetime.

3.3 Photocatalysis study

The photocatalytic activities of BCN, NCN and BCN-NCN are evaluated by monitoring the changes in the maximum absorption at 664 nm for an aqueous MB solution under visible light. Fig. 5a shows the absorption spectra of MB as blank solution as well as in presence of catalyst BCN-NCN. Before irradiation, both blank and catalyst loaded MB solution are stirred in dark for 45 min for adsorption-desorption equilibration. When light is turned off (dark reaction) and the absorption of MB is measured, blank MB shows only negligible decrease in initial concentration, whereas MB solution in presence of BCN-NCN displays a substantial decrease in initial concentration (Fig. 5b). After turning on the light source and subjecting the solution to visible light irradiation, a remarkable decrease in concentration of MB solution is observed for BCN-NCN as compared to BCN or NCN. Impressively, the direct decomposition of MB in absence of photocatalyst is not detected. The decrease in initial concentration of MB in each case is shown in Fig. 5b. The trend

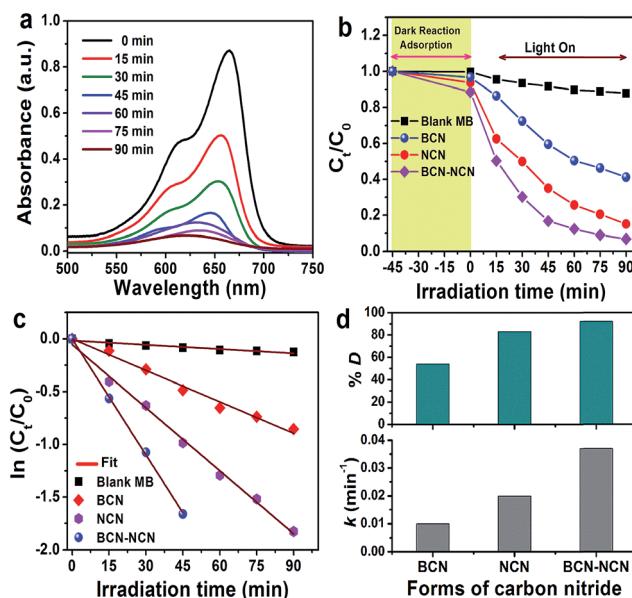


Fig. 5 (a) UV-vis absorption spectra of MB solution in presence of catalyst BCN-NCN for different time intervals of light irradiation. (b) Photodecomposition study of MB solution without (blank MB) and with catalysts (BCN, NCN, BCN-NCN) and in presence (light on) and absence (light off) of visible light. (c) Plot of $\ln\left(\frac{C_t}{C_0}\right)$ vs. irradiation (t) along with straight line fit to determine rate constants (min^{-1}). (d) Comparison of percentage of MB degraded ($\% D$) and the associated rate constant for different samples.

in the photocatalytic activities follows the trend: BCN–NCN > NCN > BCN. Fig. 5c shows the linear relationship of $\ln\left(\frac{C_t}{C_0}\right)$ vs. irradiation time (t), and the calculated values of rate constants are shown in Fig. 5d. It can be seen from Fig. 5d, about 92% of MB is photodegraded by BCN–NCN over irradiation for 90 min with associated rate constant (k) of 0.037 min^{-1} , while 83% is photodegraded by NCN for the same irradiation time with rate constant of 0.020 min^{-1} . MB removal over BCN is 54% with the lowest k value of 0.010 min^{-1} . Electron collection in $g\text{-C}_3\text{N}_4$ may have taken place by two pathways: self-sensitization of MB under visible light in which photoexcited electrons in MB are transferred to CB of $g\text{-C}_3\text{N}_4$, and the other being direct excitation of electrons to CB of C_3N_4 under visible light.³⁰ Wide band gap semiconductor, such as TiO_2 , which does not absorb visible light, self-sensitized decomposition of organic dyes under visible light is prominent. However, $g\text{-C}_3\text{N}_4$ has band gap that lies in the visible region of solar spectrum. Therefore, direct photoexcitation of electrons to CB in $g\text{-C}_3\text{N}_4$ is feasible, which further supports the fact that $g\text{-C}_3\text{N}_4$ mediated photodegradation of MB is dominating rather than self-sensitized degradation of MB. From the results, we attempt to provide some explanations for the observed differences in the photocatalytic activity of BCN, NCN and BCN–NCN in the degradation of MB. We will try to explain the possible pathways that could provide an idea of the differences in the photodegradation of MB in each of the samples. In case of BCN, as it has bulk structure, presence of large numbers of stacked layers could be expected, and the photoexcited carriers might undergo facile bulk recombination before reaching to the surface. Those carriers which could migrate to the catalyst surface could interact with less numbers of adsorbed MB dye molecule (because of the least surface area in BCN). Therefore, a reduction in photocatalysis is expected. On the other hand, NCN has a sufficiently large surface area and the numbers of available surface carriers are expected to be high on the surface because of the lowering of bulk recombination. Therefore, a large percentage of freely available carriers are available on the surface to interact with sufficient numbers of adsorbed MB molecule. Even though the surface area of BCN–NCN is lower than that of NCN, the high photocatalytic activity in BCN–NCN can be associated with its visible absorbing band gap and mostly due to the sufficiently prolonged carrier lifetime mediated by heterostructure interface.

Stability of photocatalyst is of paramount importance when practical applications of photocatalysts are concerned. Stability study was performed by recycling of photocatalytic degradation of MB on the catalysts surface for three times under visible light. We performed stability test for BCN–NCN as it exhibited highest photocatalytic activity. As Fig. 6a shows, there is no obvious photoactivity loss of MB after 3rd cycle. XRD pattern of the sample of un-irradiated BCN–NCN and that of the irradiated sample recovered after 3rd photocatalytic run is recorded, and as Fig. 6b clearly demonstrates there is no significant change in the diffraction pattern of BCN–NCN after the stability test. The small change in intensity of (002) peak can be ascribed to the

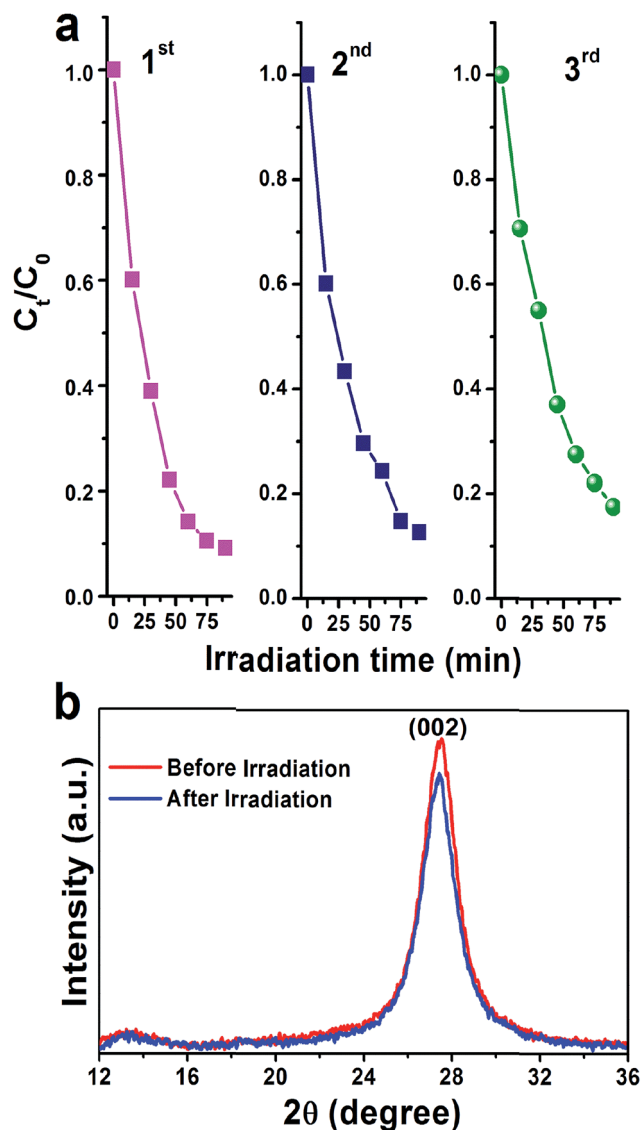


Fig. 6 (a) The photochemical stability of BCN–NCN in the photodegradation of MB with three photocyclic reaction tests. (b) XRD pattern of BCN–NCN before catalytic reaction and after 3rd photocyclic test.

presence of adsorbed MB molecule on C_3N_4 and π – π interaction between them, which after 3rd cyclic test minutely affects its crystallinity, confirming that BCN–NCN is quite a stable photocatalyst in terms of its practical applications. High photocatalytic activity of BCN–NCN may be caused by the presence of available carriers and formation of active radical species. Irradiation of MB–(BCN–NCN) solution under visible light will excite electrons from N 2p to C 2p with electrons on conduction band (CB) and holes in valence band (VB). Since the catalyst is dispersed in aqueous MB solution, the CB electrons would be able to reduce O_2 adsorbed on C_3N_4 surface to form superoxide radical ($\text{O}_2^{\cdot-}$). The photogenerated holes in VB, however, are expected to form hydroxyl radical ($\cdot\text{OH}$) by reacting with H_2O . For confirmation of the reactivity of different radicals and carriers on the photocatalysis, we used trapping experiments

(TE) by adding few radical scavengers (SV) in the MB solution catalyzed by the stable photocatalyst BCN–NCN. For the experiment, *tert*-butanol (*t*-BA) is used as hydroxyl scavenger ($\cdot\text{OH}$), ammonium oxalate (AO) and *p*-benzoquinone (BQ) for scavenging hole (h^+) and superoxide radical ($\text{O}_2^{\cdot-}$), respectively.^{31–33} It is seen in Fig. 7a that there is slight reduction in the degradation due to the addition of *t*-BA, indicating participation of less numbers of $\cdot\text{OH}$ on MB degradation. Photodegradation is slightly suppressed on adding AO to the MB solution, implying that holes play an active role in the MB decomposition. There is a dramatic decrease in MB removal on adding BQ in the solution, suggesting that $\text{O}_2^{\cdot-}$ is the most active radical species leading to the degradation of MB. The results are quite reflected in Fig. 7b. In absence of any scavengers (SV), MB degradation by BCN–NCN is 92%, while on adding BQ as $\text{O}_2^{\cdot-}$ scavengers the degradation of MB drops down to 31%.

3.4 Mechanism of photocatalytic degradation

The band edge positions (VB and CB) of BCN–NCN are of much significance to understand the interface formation, band bending and the mechanism of charge carrier separation, as well as formation of $\text{O}_2^{\cdot-}$ and $\cdot\text{OH}$ radicals. There are several reports on the band edge potential (VB and CB) of *g*- C_3N_4 in bulk and nanosheets, which is based on the results of electron spectroscopy measurement of potential with respect to SHE (standard hydrogen electrode), and theoretical calculations.^{34–38} These reports have speculated that on modification of bulk structure of C_3N_4 to few layered nanosheets the structure gets distorted, resulting in relative shifting in CB and VB edge position. For bulk and nanosheets, the CB edge potentials are found to be in between (–0.78 to –1.49 V) and VB between (1.3 to 1.86 V). Yang *et al.* observed a downward shifting of CB edge

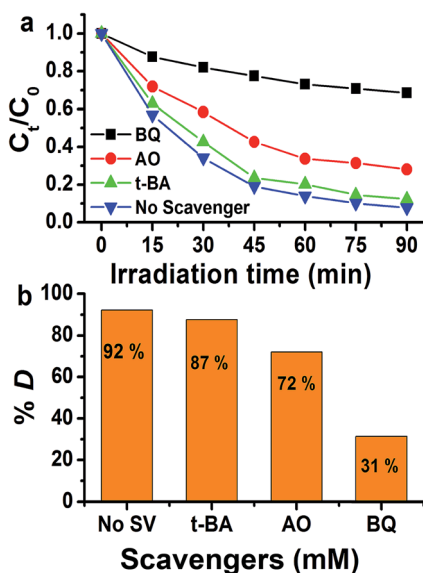


Fig. 7 (a) Photodegradation study of MB catalyzed by BCN–NCN in presence of scavenger (SV) *t*-BA ($\cdot\text{OH}$), AO (h^+) and BQ ($\text{O}_2^{\cdot-}$). (b) Degradation of MB is suppressed in presence of scavenger and lowest degradation is observed in presence of BQ scavenger.

potential from –1.49 V in bulk to –1.40 V in nanosheets of *g*- C_3N_4 .¹² Li *et al.* observed a downward shifting of CB edge potential from –1.23 V to –0.88 V and VB edge shifting from 1.31 V to 1.86 V in bulk and nanosheets, respectively.³⁶ Based on these results, we have provided a schematic band diagram (Fig. 8a and b) to show the band edge positions BCN–NCN heterostructure with respect to vacuum level as well as with reference to standard hydrogen electrode (SHE).^{34–38} Fig. 8a depicts a schematic of the conduction band (CB) and valence band (VB) edge positions in the heterostructure for the corresponding band gap values of 2.74 eV and 2.97 eV for BCN and NCN, respectively. Fig. 8b shows the band diagram of heterostructure with reference to SHE and the associated redox potential for $\cdot\text{OH}/\text{H}_2\text{O}$ and $\text{O}_2/\text{O}_2^{\cdot-}$. Because of different band alignment of VB and CB in the heterostructure, the electrons can move from CB of BCN to CB of NCN. Similarly, holes can migrate from VB of NCN to VB of BCN. The field at the interface provides the driving force in the facile separation of charge carriers, which finally become available to interact with O_2 or H_2O to form $\text{O}_2^{\cdot-}$ and $\cdot\text{OH}$ radicals. If we consider the CB edge potential in between the above mentioned values of potential, the CB edge potential is more positive than the standard redox potential of $\text{O}_2/\text{O}_2^{\cdot-}$ (–0.33 V vs. SHE). Therefore, superoxide radical can be easily formed in this process. Considering the VB edge potentials having the reported values, the position of holes in VB is at lower potential than the standard redox potential of $\cdot\text{OH}/\text{H}_2\text{O}$ (+2.27 V).^{34–38}

Both trapping experiment and band edge potentials of electrons in CB confirm that $\text{O}_2^{\cdot-}$ has major contribution in the photodegradation of MB. Superoxide radicals ($\text{O}_2^{\cdot-}$) are, however, unstable in aqueous solution and readily transform to $\cdot\text{OH}$. Formation of $\cdot\text{OH}$ from superoxide radical ($\text{O}_2^{\cdot-}$) occurs by multiple oxygen reduction reaction as shown below.³⁹

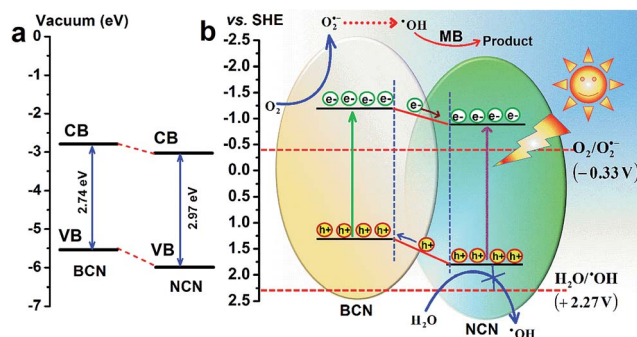
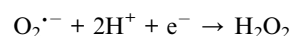
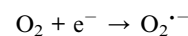


Fig. 8 (a) Schematic showing band diagram of BCN, NCN and the heterostructure relative to vacuum level. (b) Schematic of the electron–hole separation at the interface in heterostructure on exposure of the MB-catalyst to visible irradiation. Band edge positions of heterostructure and redox potential of $\cdot\text{OH}/\text{H}_2\text{O}$ and $\text{O}_2/\text{O}_2^{\cdot-}$ with respect to standard hydrogen electrode (SHE) potential are indicated.

The generated hydroxyl radicals have the propensity to react with most of the organic compounds by direct electron transfer, H abstraction, etc.

We now propose a mechanism for the degradation of MB by hydroxyl radical on the surface of BCN-NCN. It might be considered that the strong adsorption of MB on C₃N₄ could be due to strong π - π interaction between MB and C₃N₄ that strongly held the dye-solid together. Besides, MB is a cationic dye molecule and g-C₃N₄ has delocalized π electrons in the s-heptazine ring, and also contains terminal N atom with lone pair of electrons. Therefore, there is a possibility of strong cationic-anionic columbic interaction between MB with g-C₃N₄ nanosheet at the solid-dye interface. There are different stages of degradation of whole MB molecule. In MB, the terminal N-CH₃ groups which have the lowest binding energy (B.E) of 70.8 kcal mol⁻¹ is first attacked by \cdot OH radical.⁴⁰⁻⁴³ In the second step \cdot OH radicals can attack the C-S⁺=C bond (B.E \sim 76 kcal mol⁻¹) and transform this to C-S(=O)-C.⁴¹ This transformation facilitates opening up of the central aromatic ring by cleavage of N-C and S-C bond. Finally the functional groups are detached and the aromatic ring is destroyed to form the final degradation products.

4. Conclusion

In conclusion, bulk, nanosheets and isotope heterostructure composed of g-C₃N₄ exhibit tunable absorption and photoluminescence properties. Compared to bulk, nanosheets of C₃N₄ have sufficiently larger surface area with free charge carriers. Though the heterostructure shows lower specific surface area than that of the nanosheets, it has a reduced effective band gap and prolonged charge carriers lifetime. These modified forms of carbon nitride, viz. nanosheets and heterostructure, show improved photocatalytic activity in the degradation of MB under visible light. Significant improvement in the photocatalytic activity in the heterostructure is due to the suitably matching valence and conduction band levels that promote facile separation of photogenerated electrons and holes, making the carriers available for photochemical reaction. It is the photogenerated conduction band electrons in the heterostructure that facilitates the formation of active radical species \cdot OH by oxygen reduction reaction, which finally interact with functional groups and aromatic ring of MB molecule and decompose it. The development of low cost heterostructure of g-C₃N₄ for efficient visible light photocatalysis will enable wide spread applications of g-C₃N₄ in various emerging applications.

Acknowledgements

B. C. would like to thank IIT Guwahati for providing institute postdoctoral fellowship to carry out the postdoctoral research. The authors like to thank Central Instrument Facility for providing the in house characterization facilities.

References

- 1 K. Nakata and A. Fujishima, *J. Photochem. Photobiol., C*, 2012, **13**, 169–189.
- 2 R. Li, H. Kobayashi, J. Guo and J. Fan, *Chem. Commun.*, 2011, **47**, 8584–8586.
- 3 X. C. Wang, K. Maeda, A. Thomas, K. Takanabe, G. Xin, J. M. Carlsson, K. Domen and M. Antonietti, *Nat. Mater.*, 2009, **8**, 76–80.
- 4 S. C. Yan, Z. S. Li and Z. G. Zou, *Langmuir*, 2010, **26**, 3894–3901.
- 5 J. Xu, M. Shalom, F. Piersimoni, M. Antonietti, D. Neher and T. J. K. Brenner, *Adv. Opt. Mater.*, 2015, **3**, 913–917.
- 6 A. Thomas, A. Fischer, F. Goettmann, M. Antonietti, J. O. Muller, R. Schlögl and J. M. Carlsson, *J. Mater. Chem.*, 2008, **18**, 4893.
- 7 A. Schwarzer, T. Saplinova and E. Kroke, *Coord. Chem. Rev.*, 2013, **257**, 2032–2062.
- 8 F. Su, S. C. Mathew, G. Lipner, X. Fu, M. Antonietti, S. Blechert and X. Wang, *J. Am. Chem. Soc.*, 2010, **132**, 16299.
- 9 A. Du, S. Sanvito and S. C. Smith, *Phys. Rev. Lett.*, 2012, **108**, 197207.
- 10 F. Dong, Z. Wang, Y. Sun, W. K. Ho and H. Zhang, *J. Colloid Interface Sci.*, 2013, **401**, 70–79.
- 11 Y. Li, Y. Sun, F. Dong and W. K. Ho, *J. Colloid Interface Sci.*, 2014, **436**, 29–36.
- 12 S. Yang, Y. Gong, J. Zhang, L. Zhan, L. Ma, Z. Fang, R. Vajtai, X. Wang and P. M. Ajayan, *Adv. Mater.*, 2013, **25**, 2452–2456.
- 13 P. Niu, L. Zhang, G. Liu and H. M. Cheng, *Adv. Funct. Mater.*, 2012, **22**, 4763–4770.
- 14 Y. Chen, B. Wang, S. Lin, Y. Zhang and X. Wang, *J. Phys. Chem. C*, 2014, **118**, 29981–29989.
- 15 Y. C. Lu, J. Chen, A. J. Wang, N. Bao, J. J. Feng, W. Wang and L. Shao, *J. Mater. Chem. C*, 2015, **3**, 73–78.
- 16 J. Zhou, M. Zhang and Y. Zhu, *Phys. Chem. Chem. Phys.*, 2014, **16**, 17627–17633.
- 17 J. Zhang, M. Zhang, R. Q. Sun and X. Wang, *Angew. Chem., Int. Ed.*, 2012, **51**, 10145.
- 18 F. Dong, Z. Li, P. Li and Z. Wu, *New J. Chem.*, 2015, **39**, 4737–4744.
- 19 Z. Zhao, Y. Sun and F. Dong, *Nanoscale*, 2015, **7**, 15–37.
- 20 X. Zhang, X. Xie, H. Wang, J. Zhang, B. Pan and Y. Xie, *J. Am. Chem. Soc.*, 2013, **135**, 18.
- 21 Z. Wang, W. Guan, Y. Sun, F. Dong, Y. Zhou and W. K. Ho, *Nanoscale*, 2015, **7**, 2471–2479.
- 22 F. Dong, Z. Zhao, T. Xiong, Z. Ni, W. Zhang, Y. Sun and W. K. Ho, *ACS Appl. Mater. Interfaces*, 2013, **5**, 11392–11401.
- 23 J. Xu, L. Zhang, R. Shi and Y. Zhu, *J. Mater. Chem. A*, 2013, **1**, 14766–14772.
- 24 Y. Li, J. Zhang, Q. Wang, Y. Jin, D. Huang, Q. Cui and G. Zou, *J. Phys. Chem. B*, 2010, **114**, 9429–9434.
- 25 H. Zhang and A. Yu, *J. Phys. Chem. C*, 2014, **118**, 11628–11635.
- 26 G. A. Meek, A. D. Baczewski, D. J. Little and B. G. Levine, *J. Phys. Chem. C*, 2014, **118**, 4023–4032.
- 27 J. Bian, J. Li, S. Kalytchuk, Y. Wang, Q. Li, T. Lau, T. A. Niehaus, A. L. Rogach and R. Q. Zhang, *ChemPhysChem*, 2015, **16**, 954–959.

- 28 C. Merschjann, T. Tyborski, S. Orthmann, F. Yang, K. Schwarzburg, M. Lublow, M. Ch, L. Steiner and T. S. Niedrig, *Phys. Rev. B: Condens. Matter Mater. Phys.*, 2013, **87**, 205204.
- 29 P. Niu, G. Liu and H. M. Cheng, *J. Phys. Chem. C*, 2012, **116**, 11013–11018.
- 30 T. Lv, L. Pan, X. Liu, T. Lu, G. Zhu, Z. Sun and C. Q. Sun, *Catal. Sci. Technol.*, 2012, **2**, 754–758.
- 31 Y. Yang, Y. Guo, F. Liu, X. Yuan, Y. Guo, S. Zhang, W. Guo and M. Huo, *Appl. Catal., B*, 2013, **142–143**, 828–837.
- 32 F. T. Li, Y. Zhao, Q. Wang, X. J. Wang, Y. J. Hao, R. H. Liu and D. Zhao, *J. Hazard. Mater.*, 2015, **283**, 371–381.
- 33 Y. Sun and J. J. Pignatello, *Environ. Sci. Technol.*, 1995, **29**(8), 2065–2072.
- 34 S. Chu, Y. Wang, Y. Guo, J. Feng, C. Wang, W. Luo, X. Fan and Z. Zou, *ACS Catal.*, 2013, **3**, 912–919.
- 35 J. Xiao, Y. Xie, F. Nawaz, S. Jin, F. Duan, M. Li and H. Cao, *Appl. Catal., B*, 2016, **181**, 420–428.
- 36 H. J. Li, B. W. Sun, L. Sui, D. J. Qian and M. Chen, *Phys. Chem. Chem. Phys.*, 2015, **17**, 3309–3315.
- 37 H. Z. Wu, L. M. Liu and S. J. Zhao, *Phys. Chem. Chem. Phys.*, 2014, **16**, 3299–3304.
- 38 X. Fan, L. Zhang, M. Wang, W. Huang, Y. Zhou, M. Li, R. Cheng and J. Shi, *Appl. Catal., B*, 2016, **182**, 68–73.
- 39 G. Xin and Y. Meng, *J. Chem.*, 2013, **2013**, 1–5.
- 40 Q. Wang, S. Tian and P. Ning, *Ind. Eng. Chem. Res.*, 2014, **53**, 643–649.
- 41 F. Huang, L. Chen, H. Wang and Z. Yan, *Chem. Eng. J.*, 2010, **162**, 250–256.
- 42 H. Lachheb, E. Puzenat, A. Houas, M. Ksibi, E. Elaloui, C. Guillard and J. M. Herrmann, *Appl. Catal., B*, 2002, **39**, 75–90.
- 43 A. Houas, H. Lachheb, M. Ksibi, E. Elaloui, C. Guillard and J. M. Herrmann, *Appl. Catal., B*, 2001, **31**, 145–157.